

SCIENTIFIC REPORTS

OPEN

Hierarchical Sheet-on-Sheet $\text{ZnIn}_2\text{S}_4/\text{g-C}_3\text{N}_4$ Heterostructure with Highly Efficient Photocatalytic H_2 production Based on Photoinduced Interfacial Charge Transfer

Zhenyi Zhang, Kuichao Liu, Zhiqing Feng, Yanan Bao & Bin Dong

We have realized *in-situ* growth of ultrathin ZnIn_2S_4 nanosheets on the sheet-like $\text{g-C}_3\text{N}_4$ surfaces to construct a “sheet-on-sheet” hierarchical heterostructure. The as-synthesized $\text{ZnIn}_2\text{S}_4/\text{g-C}_3\text{N}_4$ heterojunction nanosheets exhibit remarkably enhancement on the photocatalytic activity for H_2 production. This enhanced photoactivity is mainly attributed to the efficient interfacial transfer of photoinduced electrons and holes from $\text{g-C}_3\text{N}_4$ to ZnIn_2S_4 nanosheets, resulting in the decreased charge recombination on $\text{g-C}_3\text{N}_4$ nanosheets and the increased amount of photoinduced charge carriers in ZnIn_2S_4 nanosheets. Meanwhile, the increased surface-active-sites and extended light absorption of $\text{g-C}_3\text{N}_4$ nanosheets after the decoration of ZnIn_2S_4 nanosheets may also play a certain role for the enhancement of photocatalytic activity. Further investigations by the surface photovoltage spectroscopy and transient photoluminescence spectroscopy demonstrate that $\text{ZnIn}_2\text{S}_4/\text{g-C}_3\text{N}_4$ heterojunction nanosheets considerable boost the charge transfer efficiency, therefore improve the probability of photoinduced charge carriers to reach the photocatalysts surfaces for highly efficient H_2 production.

Photocatalytic H_2 production through water splitting or reduction has received great attention in recent years, since it offers an economical and environmentally friendly strategy to convert solar energy into preservable chemical fuels for mitigating the excessive consumption of non-sustainable fossil fuels such as coal, petroleum and natural gas^{1–4}. To date, various kinds of UV- or visible-response semiconductors, such as TiO_2 , ZnO , Cu_2O , CdS , and so forth, have been developed as photocatalysts for H_2 production due to their suitable band potential and catalytic functions^{5–10}. Besides these traditional semiconductor photocatalysts, a large number of semiconductive materials, including metal-organic frameworks (MOFs), polyoxometalate (POM), and metal free compounds, are also being introduced as potential candidates for the new generation of photocatalysts to fulfill the photocatalytic water reduction and oxidation^{11–14}. Among them, the two-dimensional (2D) layered polymer, graphitic carbon nitride ($\text{g-C}_3\text{N}_4$), is considered as the most promising visible-light-active photocatalyst because of its unique electronic structure, high stability, nontoxic nature, and low cost^{15–17}. However, the photocatalytic activity on H_2 production over single-component $\text{g-C}_3\text{N}_4$ so far is unsatisfactory due to its limited surface areas, poor light-harvesting efficiency and fast recombination of photoinduced charge carriers^{15,17}. To overcome the above drawbacks, much effort has been devoted to the construction of multi-component heterostructural photocatalysts through coupling other visible-active semiconductor with $\text{g-C}_3\text{N}_4$ nanosheets, in which the heterogeneous interfaces can effectively assist the photoinduced charge-carriers migration and hinder these charge-carriers recombination to enhance the photocatalytic efficiency^{18–24}. Moreover, the surface structures and light-harvesting

Key Laboratory of New Energy and Rare Earth Resource Utilization of State Ethnic Affairs Commission, School of Physics and Materials Engineering, Dalian Nationalities University, 18 Liaohe West Road, Dalian 116600, P. R. China. Correspondence and requests for materials should be addressed to B.D. (email: dong@dlnu.edu.cn)

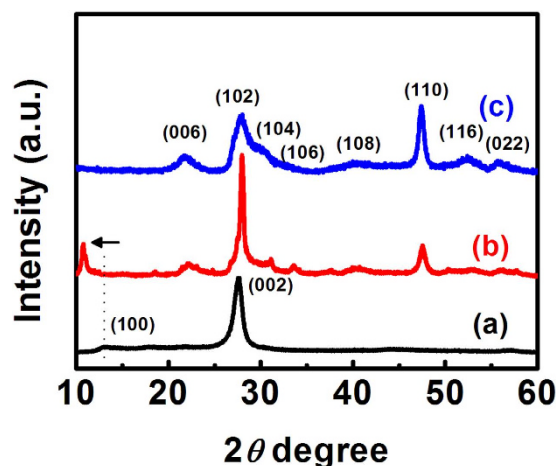


Figure 1. XRD patterns of the as-synthesized samples: (a) g-C₃N₄ nanosheets; (b) 15 wt% ZnIn₂S₄/g-C₃N₄ heterojunction nanosheets; (c) ZnIn₂S₄ nanosheets.

behavior can be also promoted through tailoring the secondary nanostructures of heterostructural photocatalysts^{25–27}. Therefore, design and architecture of g-C₃N₄-based heterostructural photocatalysts with the matchable bandgap, desired component, and hierarchical nanostructures is still the hot topics in the field of solar-to-fuels conversion.

As an important ternary chalcogenide semiconductor, hexagonal phase ZnIn₂S₄ with 2D layered structure and narrow bandgap has been extensively investigated in photocatalysis, especially serving as the photosynergistic components in heterojunction photocatalysts to enhance the photocatalytic efficiency for H₂ production^{28–32}. In the viewpoint of band structure, the bandgap of ZnIn₂S₄ ($E_g^{\text{ZnIn}_2\text{S}_4} \sim 2.6$ eV) is smaller than that of g-C₃N₄ ($E_g^{\text{g-C}_3\text{N}_4} \sim 2.8$ eV) while the conduction band (CB) of ZnIn₂S₄ ($E_{\text{CB}}^{\text{ZnIn}_2\text{S}_4} = -1.0$ V) is higher than that of g-C₃N₄ ($E_{\text{CB}}^{\text{g-C}_3\text{N}_4} = -1.1$ V)^{15,17,28,33}. Accordingly, when integrating of ZnIn₂S₄ nanostructure with g-C₃N₄ nanosheets, a “type I” heterojunction would be formed in their interface, meaning that the CB and valence band (VB) positions of g-C₃N₄ straddle those of ZnIn₂S₄. As such, the ZnIn₂S₄ can be seemed as a “charge sink” to accept the photoinduced charge carriers from adjacent g-C₃N₄, leading to the improvement of charge separation on g-C₃N₄ and thereby enhancing its photocatalytic activity. On the other hand, the 2D sheet-like ZnIn₂S₄ nanostructures could be easily anchored onto the active or flexible 2D substrates, such as F-doped SnO₂ (FTO) thin film and reduced graphene oxide (RGO) nanosheets, to form the “sheet-on-sheet” type heterostructure. This kind of hierarchical nanostructure usually exhibits a high surface area, strong light harvesting, and efficient charge mobility due to its unique structure advantages^{25,26,29,31,33,34}. The above analysis implies that once the ZnIn₂S₄ nanosheets combine with g-C₃N₄ nanosheets, a significant enhancement on photocatalytic H₂ production may be realized through synergistic promotion on the inner charge carriers and outer hierarchical structures. However, little effort has been donated to the synthesis of ZnIn₂S₄/g-C₃N₄ heterostructure toward the highly efficient photocatalytic H₂ production. Herein, we report a novel kind of “sheet-on-sheet” heterostructure synthesized through *in-situ* growth of ultrathin ZnIn₂S₄ nanosheets onto g-C₃N₄ nanosheets surfaces. After introducing the ZnIn₂S₄ nanosheets, the specific surface area of g-C₃N₄ nanosheets is obviously promoted, resulting in providing the more active sites for the photoreaction. Furthermore, the intimate contacted interface between the ZnIn₂S₄ and g-C₃N₄ nanosheets facilitates the photoinduced charge-carriers transfer from g-C₃N₄ to ZnIn₂S₄ based on the heterojunction effect. By taking of the above features, the as-synthesized ZnIn₂S₄/g-C₃N₄ heterojunction nanosheets exhibit a significantly enhanced visible-light photocatalytic H₂ production performance as compared to the single component of ZnIn₂S₄ or g-C₃N₄ nanosheets.

Results

X-ray diffraction (XRD) patterns of the as-synthesized samples are shown in Fig. 1. Two pronounced diffraction peaks appear at 13.1° and 27.4° for g-C₃N₄ nanosheets, reflecting to the periodic structure of intra-planar tri-s-triazine packing as the (100) peak, and the interlayer stacking of conjugated aromatic structures as the (002) peak for graphitic materials, respectively^{11,15,17}. The diffraction peaks of ZnIn₂S₄ nanosheets can be perfectly indexed as a pure hexagonal phase of ZnIn₂S₄ (JCPDS No. 65–2023)^{28,29,31}. In the case of ZnIn₂S₄/g-C₃N₄ heterojunction nanosheets, the XRD pattern shows diffraction peaks of both ZnIn₂S₄ and g-C₃N₄ nanosheets, while the feature peaks of ZnIn₂S₄ (27.7°) and g-C₃N₄ (27.4°) are very close and overlap with each other. Note that the diffraction peaks of ZnIn₂S₄ nanosheets are very weak. This phenomenon may be ascribed to two reasons: (1) the ultrathin 2D nanostructure of ZnIn₂S₄, leading to the ultra-small size in its c-axis orientation³¹; (2) the low content of ZnIn₂S₄ component in the heterostructure²⁵. Besides, after introducing the ZnIn₂S₄ by hydrothermal method, the (100) diffraction peak of g-C₃N₄ becomes more intense, and its position shifts toward the lower diffraction angle (10.8°) (Figure S1). This reveals that some metal ions from ZnIn₂S₄ surfaces may be connected with the g-C₃N₄ through the lone-pair electrons of nitrogen in the “nitrogen pots”, thus leading to enlarging the intra-planar separation of ordered tri-s-triazine packing^{21,22,35}. Moreover, some weak peaks corresponded to the

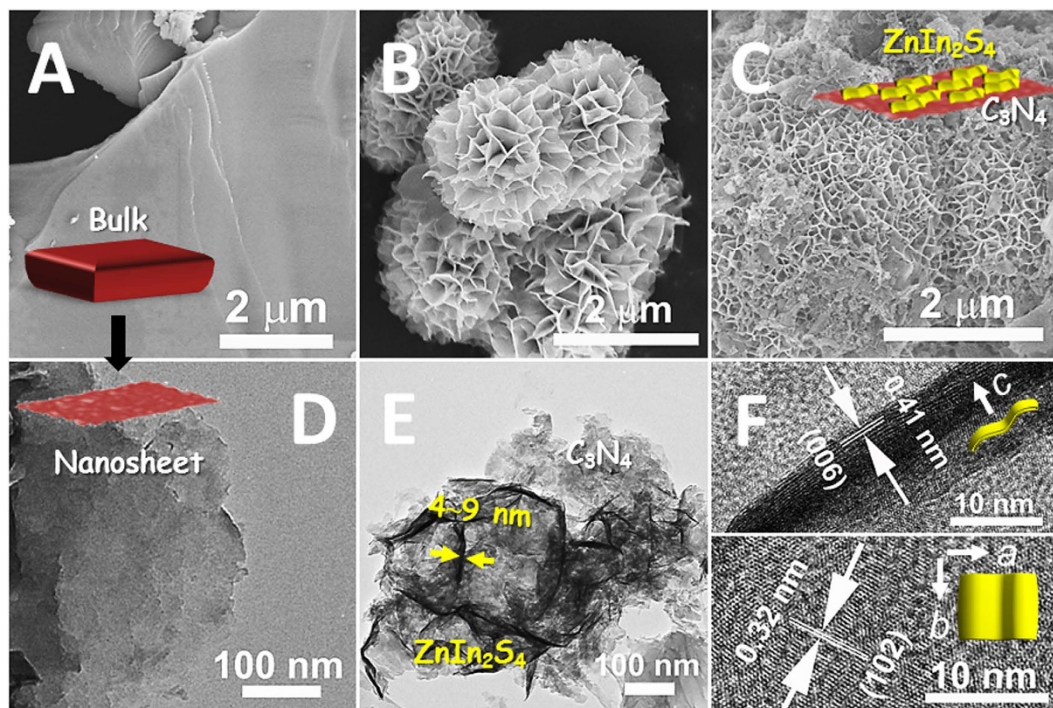


Figure 2. SEM images of (A) bulk g-C₃N₄, (B) ZnIn₂S₄ nanosheets, and (C) ZnIn₂S₄/g-C₃N₄ heterojunction nanosheets; TEM images of (D) the exfoliated g-C₃N₄ nanosheet and (E) 15 wt% ZnIn₂S₄/g-C₃N₄ heterojunction nanosheets; (F) HRTEM images of the side view and top view of ZnIn₂S₄ nanosheet grown on the g-C₃N₄ nanosheets. Insets showing structure schematic diagrams of the corresponding samples.

intermediates of thermal polymerized g-C₃N₄ are also detected on the XRD pattern of ZnIn₂S₄/g-C₃N₄ heterojunction nanosheets, implying that a small part of g-C₃N₄ nanosheets might be further exfoliated (or reduced) into the structural units of g-C₃N₄, such as melamine, ammeline, or tri-s-triazine units, due to the longer reaction time for hydrothermal growth of ZnIn₂S₄ onto g-C₃N₄ nanosheets^{16,36}.

Scanning electron microscopy (SEM) and transmission electron microscopy (TEM) images were performed to directly observe the morphologies and structures of the ZnIn₂S₄/g-C₃N₄ heterojunction nanosheets in comparison with the single component of ZnIn₂S₄ and g-C₃N₄ nanosheets, as displayed in Fig. 2. The thermal polymerized g-C₃N₄ shows a bulk structure with smooth surfaces (Fig. 2A), which can be easily exfoliated into the wrinkled sheet-like nanostructures by the ultrasonic treatment in methanol solution (Fig. 2D). Figure 2B reveals significant aggregation of the nanosheets into microspheres with the average diameter of ~1.5 μm for the hydrothermally synthesized ZnIn₂S₄ sample. Interestingly, when introducing the as-fabricated g-C₃N₄ nanosheets as the substrates during the hydrothermal process, the ZnIn₂S₄/g-C₃N₄ heterojunction nanosheets could be achieved in the form of “sheet-on-sheet” structure (Figure S2 and Figure S3). As observed in Fig. 2C, the layered surfaces of g-C₃N₄ nanosheet are covered with the high density of secondary ZnIn₂S₄ nanosheets. These nanosheets with uniformly ultrathin 2D-structure are connected and even across to each other, finally forming the sheet-like networks vertically aligned on the g-C₃N₄ nanosheet surface. This kind of unique hierarchical heterostructure (65.9 m² g⁻¹) shows much higher specific-surface-area than the general sheet-like structure for pure g-C₃N₄ (12.8 m² g⁻¹), thereby providing more active sites for the photocatalytic reaction (Figure S4). Moreover, the interspaces among interweaved ZnIn₂S₄ nanosheets on the g-C₃N₄ nanosheets may also boost the light-harvesting behavior of this hierarchical heterostructure though the multi-reflection processes on the incident electromagnetic waves^{25,26,29}. TEM image of the ZnIn₂S₄/g-C₃N₄ heterojunction nanosheets further confirms that the ultrathin ZnIn₂S₄ nanosheets with thickness of 4~9 nm are vertically grown onto the g-C₃N₄ nanosheets surface (Fig. 2E and Figure S3). Figure 2F presents the high-resolution (HR) TEM of an individual ZnIn₂S₄ nanosheet on g-C₃N₄ surface, in which the lattice-fringe spacing of 0.41 nm appeared on the side view (perpendicular sheet) can be assigned to the (006) crystal plane of hexagonal ZnIn₂S₄, while the top view (planar sheet) image shows the interplanar distances of 0.32 nm, belonging to the *d*-spacing of (102) planes of hexagonal ZnIn₂S₄. In short, intimate contacted heterojunctions between ZnIn₂S₄ and g-C₃N₄ nanosheets are indeed constructed by the *in-situ* growth process, which may be beneficial for the photoinduced interfacial charge-transfer from g-C₃N₄ to ZnIn₂S₄.

Figure 3A presents the Fourier transform infrared (FT-IR) spectra of the as-synthesized ZnIn₂S₄/g-C₃N₄ heterojunction nanosheets along with the single ZnIn₂S₄ and g-C₃N₄ nanosheets for the purpose of structure comparison. The stretching vibration bands on the spectra of g-C₃N₄ nanosheets show characteristics similar to those of the reported results^{13,16,21,23}. Accordingly, the peaks appeared between 1200 cm⁻¹ and 1650 cm⁻¹ are attributed to the stretching vibration modes of CN heterocycles. The peak located at 3200 cm⁻¹ is originated to the NH stretching vibration mode, while the 811 cm⁻¹ to the feature vibration mode of *s*-triazine ring unit. For the ZnIn₂S₄ sample, only two peaks at 1396 cm⁻¹ and 1610 cm⁻¹, belonging to the surface hydroxyl groups

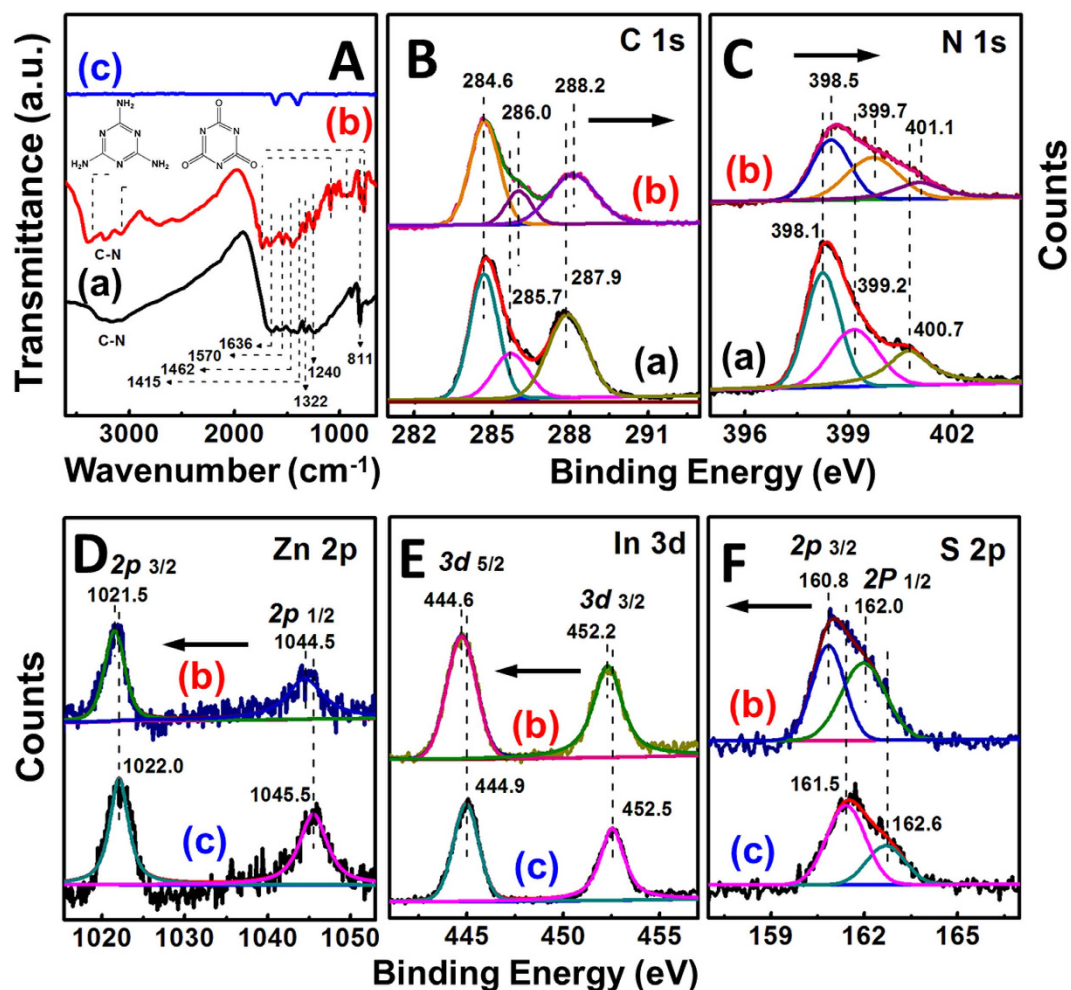


Figure 3. (A) FT-IR spectra of the as-synthesized samples: (a) g-C₃N₄ nanosheets, (b) 15 wt% ZnIn₂S₄/g-C₃N₄ heterojunction nanosheets, and (c) ZnIn₂S₄ nanosheets; XPS spectra of the as-synthesized samples: (B) C 1s core-level spectra; (C) N 1s core-level spectra: (a) g-C₃N₄ nanosheets, (b) 15 wt% ZnIn₂S₄/g-C₃N₄ heterojunction nanosheets; (D) Zn 2p core-level spectra; (E) In 3d core-level spectra; (F) S 2p core-level spectra: (b) 15 wt% ZnIn₂S₄/g-C₃N₄ heterojunction nanosheets, and (c) ZnIn₂S₄ nanosheets.

and absorbed water molecules, can be observed on the FT-IR spectrum²⁵. After the growth of ZnIn₂S₄ nanosheets onto g-C₃N₄ surfaces, the heterojunction nanosheets show the typical stretching vibration modes of both ZnIn₂S₄ and g-C₃N₄ nanosheets. Besides, a series of new vibration bands can be detected simultaneously on the spectrum of ZnIn₂S₄/g-C₃N₄ nanosheets, which are in agreement with the vibration bands of melamine and/or ammeline^{16,36}. This further suggests that during the long-time hydrothermal process, a few number of g-C₃N₄ nanosheets were exfoliated (or reduced) into the sub-structures of g-C₃N₄. To study in-depth the chemical configurations of the as-synthesized samples, the X-ray photoelectron spectroscopy (XPS) analyses were performed. As observed in Fig. 3B, three main peaks with the binding energies at 284.6 eV, 285.7 eV, and 287.9 eV can be found on the C 1s core-level spectrum of g-C₃N₄ nanosheets, which are assigned to sp² C-C bonds of graphitic carbon, sp³-coordinated carbon bonds, and sp²-bonded carbon (N-C=N) of the s-triazine rings, respectively^{17,21}. The binding energy for the C 1s peak at 284.6 eV can be attributed to the adventitious carbon species on the samples and the carbon-containing contaminants, which was used as the reference for calibration. The N 1s signal of g-C₃N₄ nanosheets also shows three feature peaks, corresponding to the sp²-bonded N (C-N=C) (398.1 eV), tertiary nitrogen N-(C)₃ groups (399.2 eV), and amino groups (C-N-H) (400.7 eV)^{17,21}. Investigations found that the relative intensity of the peaks relating to the N-C=N and C-N=C groups of g-C₃N₄ nanosheets are decreased after hydrothermal treatment for a long time, indicating that some of the tri-s-triazine units of g-C₃N₄ were distorted during this process. Meanwhile, when introducing the ZnIn₂S₄ nanosheets onto g-C₃N₄ nanosheets to form the heterojunction, both the C 1s and N 1s characteristic signals of g-C₃N₄ nanosheets shift slightly toward the higher binding energy side. On the contrary, the binding energies of Zn 2p (1022.0 eV for 2p_{3/2} and 1045.5 eV for 2p_{1/2}), In 3d (444.9 eV for 3d_{5/2} and 452.5 eV for 3d_{3/2}), and S 2p (161.5 eV for 2p_{3/2} and 162.6 eV for 2p_{1/2}) for the ZnIn₂S₄/g-C₃N₄ heterojunction nanosheets are a little lower than the corresponding values for the pure ZnIn₂S₄ nanosheets^{25,29,31}, as shown in Fig. 3D–F. The binding energy shifts for the heterojunction components could be explained by a strong interaction between ZnIn₂S₄ and g-C₃N₄ nanosheets^{21,37–39}. Theoretically, the enhancement

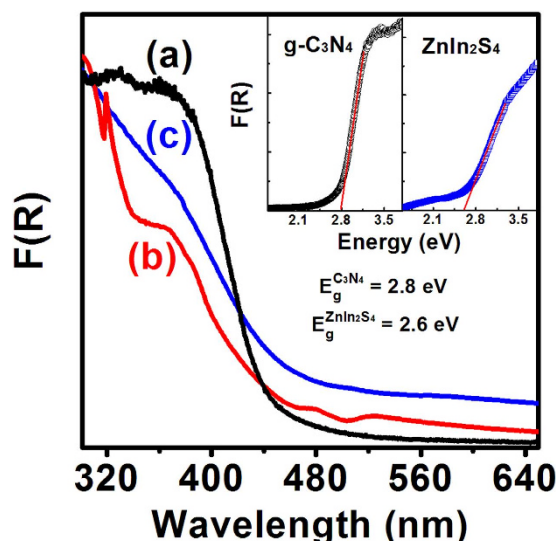


Figure 4. UV-Vis absorption spectra of the as-synthesized samples: (a) g-C₃N₄ nanosheets, (b) 15 wt% ZnIn₂S₄/g-C₃N₄ heterojunction nanosheets, and (c) ZnIn₂S₄ nanosheets; insets showing the plots of the F(R) versus energy for the g-C₃N₄ and ZnIn₂S₄ nanosheets.

of binding energy means the weakened electron screening effect caused by the decreased electron concentration, while the increase in electron concentration leads to the decrease of binding energy due to the promoted electron screening effect. Thus, in this case, it is reasonable to conclude that the higher and lower binding energy shifts are ascribed to the decreased electron concentration of g-C₃N₄ nanosheets and increased electron concentration of ZnIn₂S₄ nanosheets due to the strong interaction between the g-C₃N₄ to ZnIn₂S₄ nanosheets based on the interfacial charge transfer.

The optical properties of the as-synthesized samples were investigated through UV-vis absorption spectra which converted from the corresponding diffuse reflectance (DR) spectra by means of the Kubelka-Munk function. As shown in Fig. 4, the absorption edges of g-C₃N₄ and ZnIn₂S₄ nanosheets appears at ~443 and ~476 nm, corresponding to the band energies of ~2.8 and ~2.6 eV, respectively. These values are consistent with the reported values of g-C₃N₄ and ZnIn₂S₄ nanosheets^{15,17–19,28,33,34}. In the case of ZnIn₂S₄/g-C₃N₄ heterojunction nanosheets, two obvious absorption bands ascribed to the characteristic absorption of g-C₃N₄ and ZnIn₂S₄ nanosheets can be found on the absorption curve of Fig. 4b. Moreover, the absorption peaks of ZnIn₂S₄ nanosheets become more intense with increase of ZnIn₂S₄ content in the heterojunction nanosheets (Figure S5), further confirming that the ZnIn₂S₄/g-C₃N₄ heterojunction nanosheets with controllable component contents were obtained.

Discussion

Photocatalytic H₂ production activities of the as-synthesized samples were evaluated under visible light ($\lambda > 400$ nm) irradiation by using triethanolamine (TEOA) as the sacrificial reagent to quench the photoinduced holes. The H₂ production rates of pure g-C₃N₄ nanosheets, pure ZnIn₂S₄ nanosheets, and ZnIn₂S₄/g-C₃N₄ heterojunction nanosheets with various ZnIn₂S₄ ratios are summarized in Fig. 5A, in which the heterojunction nanosheets show the enhanced H₂ production rates as compared to the single heterojunction components. It implies that *in-situ* growth of ZnIn₂S₄ nanosheets onto g-C₃N₄ nanosheets could noticeably improve the photocatalytic activities on H₂ production. Even with only 2.5 wt% ZnIn₂S₄ nanosheets, the heterojunction nanosheet displays a H₂ production rate of 5.2 $\mu\text{mol h}^{-1}$, which is more than 6 times higher than that of pure g-C₃N₄ nanosheets (0.8 $\mu\text{mol h}^{-1}$). The poor photoactivity of g-C₃N₄ nanosheets for the H₂ production is mainly ascribed to its limited light-harvesting efficiency and fast recombination of photoinduced charge carriers^{18,19}. The optimal photocatalytic activity was achieved on 15 wt% ZnIn₂S₄ with a H₂ production rate of 14.1 $\mu\text{mol h}^{-1}$. This value is ~17.6 times higher than that of pure g-C₃N₄ nanosheets and even nearly 4 times higher than that of the pure ZnIn₂S₄ nanosheets. Accordingly, the apparent quantum efficiency of this optimal sample is estimated as 0.28% under irradiation at 420 nm. Note that only 5 mg of 15 wt% ZnIn₂S₄/g-C₃N₄ heterojunction nanosheets was used for H₂ production in our work. However, when the ZnIn₂S₄ content is higher than 15 wt%, a further increase in ZnIn₂S₄ content (20 wt%) leads to a rapid decrease in the photocatalytic activity for H₂ production. This photoactivity reduction can be attributed to the increased opacity (so-called shield effect), resulting in a decrease of irradiation passing through the suspension photoreaction solution^{21,25,29,31,40,41}. As observed in Fig. 5B, the significant enhancement of photocatalytic activity for the heterojunction sample can be further confirmed by the time-dependent H₂ production behaviors. It could be found that the H₂ production amounts linearly increases with the irradiation time. After visible light irradiation for 2 h, the H₂ production yield of 15 wt% ZnIn₂S₄-decorated g-C₃N₄ nanosheet could reach 28.2 μmol , which is greatly superior to the pure g-C₃N₄ and ZnIn₂S₄ nanosheets. The enhanced photoactivity on H₂ production could be explained by two main reasons: (1) the reduced recombination process of photoinduced charge carriers on g-C₃N₄ and increased amount of charge carriers on ZnIn₂S₄ based on the interfacial charge transfer; (2) the higher specific-surface-area and enhanced light absorption for

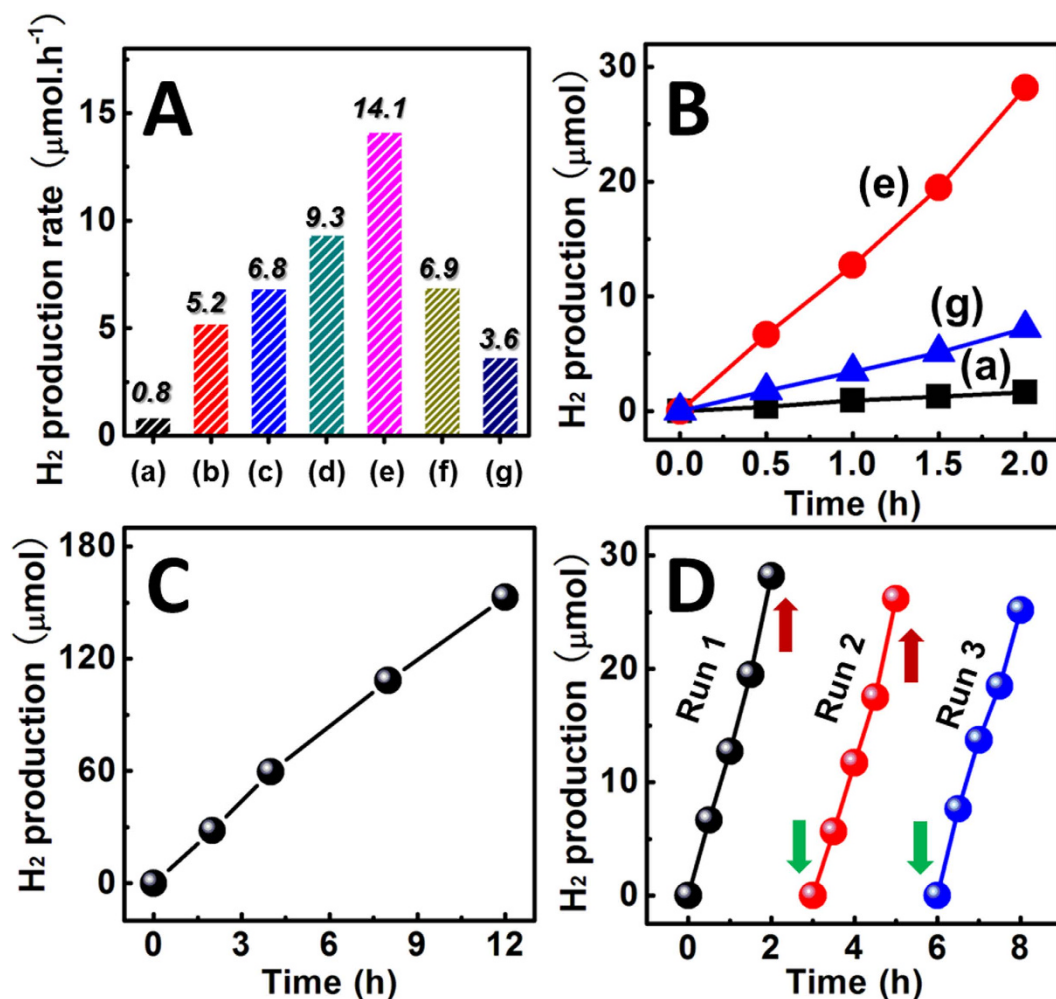


Figure 5. (A) Photocatalytic H₂ production under visible light irradiation over (a) g-C₃N₄ nanosheets; (e) 15 wt% ZnIn₂S₄/g-C₃N₄ heterojunction nanosheets, and (g) ZnIn₂S₄ nanosheets; (B) comparison of visible-light-driven H₂ production rate over different samples: (a) g-C₃N₄ nanosheets, (b) 2.5 wt%, (c) 5 wt%, (d) 10 wt%, (e) 15 wt%, (f) 20 wt% ZnIn₂S₄/g-C₃N₄ heterojunction nanosheets, and (g) ZnIn₂S₄ nanosheets; (C) photocatalytic H₂ production curve with prolonged irradiation time over 15 wt% ZnIn₂S₄/g-C₃N₄ heterojunction nanosheets; (D) cycling test of photocatalytic H₂ production over 15 wt% ZnIn₂S₄/g-C₃N₄ heterojunction nanosheets.

the unique “sheet-on-sheet” heterostructure as aforementioned. However, it should be point out that in comparison with the pure ZnIn₂S₄ nanosheets (132.0 m² g⁻¹), the heterojunction nanosheets (65.9 m² g⁻¹) shows the lower specific-surface-area, but the higher photoactivity. Meanwhile, the g-C₃N₄ nanosheets treated by the hydrothermal process in the absence of ZnIn₂S₄ precursor show a lower photocatalytic H₂ production rate (0.41 μmol/h) as compared to the pure (untreated) g-C₃N₄ nanosheets (Figure S6), because of the poor photoactivities of the exfoliation or reduction of g-C₃N₄ with the ultra-small structures, such as melamine, ammeline, or tri-s-triazine units^{16,36}. These observations also the indirect evidence that the dynamics process of photoinduced charge transfer occurring on the interface between the ZnIn₂S₄ and g-C₃N₄ nanosheets may be crucial to the photocatalytic H₂ production activities of heterojunction nanosheets. At low ZnIn₂S₄ content, a well dispersion of ZnIn₂S₄ nanosheets on the g-C₃N₄ nanosheets could be formed. In this way, the increase of ZnIn₂S₄ content would induce more ZnIn₂S₄ nanosheets assembled onto the g-C₃N₄ surface, which generates larger contact area between the ZnIn₂S₄ and g-C₃N₄ nanosheets, thereby allowing more efficient interfacial charge transfer. However, excess ZnIn₂S₄ loading causes considerable reduction of light absorption for the covered g-C₃N₄, and decreases its excitation process for interfacial charge transfer. Therefore, a balance would be built between ZnIn₂S₄ loading amount and ZnIn₂S₄/g-C₃N₄ contact area, which can maximize the photocatalytic H₂ production for the heterojunction nanosheets. Through the sequential remediation of heterojunction components, we concluded an optimal loading of 15 wt% ZnIn₂S₄ onto g-C₃N₄, which exhibited the highest photocatalytic activity in our work.

Besides, this optimal ZnIn₂S₄/g-C₃N₄ heterojunction nanosheets also shows fairly stable photoactivity for H₂ production. In Fig. 5C, the H₂ production rate remains consistent even at the prolonged time period for 12 h. Meanwhile, the recycling ability for the 15 wt% ZnIn₂S₄/g-C₃N₄ heterojunction nanosheets was further studied by performing a three-run test of photocatalytic H₂ production. Figure 5D shows that no notable decreases

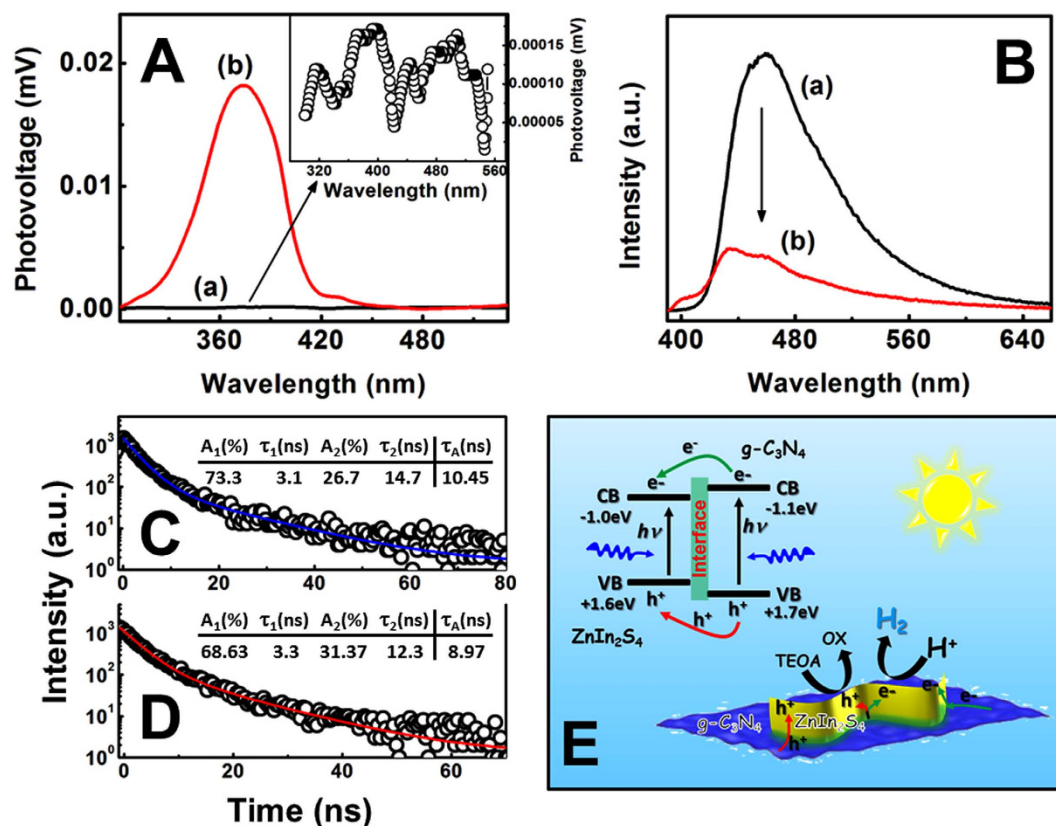


Figure 6. (A) SPS of the as-synthesized samples: (a) g-C₃N₄ nanosheets, (b) 15 wt% ZnIn₂S₄/g-C₃N₄ heterojunction nanosheets; (B) steady-state PL spectra of (a) g-C₃N₄ nanosheets and (b) 15 wt% ZnIn₂S₄/g-C₃N₄ heterojunction nanosheets; Time-resolved transient PL decay of (C) g-C₃N₄ nanosheets and (D) 15 wt% ZnIn₂S₄/g-C₃N₄ heterojunction nanosheets; (E) schematic diagram showing the photoinduced charge transfer in the interface between ZnIn₂S₄ and g-C₃N₄ nanosheets.

of H₂ evolution were detected during the three-run test, powerfully verifying the good stability of 15 wt% ZnIn₂S₄/g-C₃N₄ heterojunction nanosheets for using as the photocatalysts.

To provide more evidence on the photoinduced charge transfer occurring in the heterojunction interface, the surface photovoltage spectroscopy (SPS) and photoluminescence (PL) spectroscopy of ZnIn₂S₄/g-C₃N₄ heterojunction nanosheets were investigated in comparison with those of pure g-C₃N₄ nanosheets. As shown in the inset of Fig. 6A, a poor response appears on the SPS curve of pure g-C₃N₄ nanosheets, indicating very low efficiency on the photovoltaic conversion. However, the photon absorption and conversion processes have been proven by the photoelectrochemistry in our previous work⁴². Thus, the low photovoltage of g-C₃N₄ nanosheets can be attributed to the Schottky interface contact between the g-C₃N₄ and ITO glass in the absence of electrolyte, which leads to the limited electron transfer process from the g-C₃N₄ to ITO glass electrode. After decoration of ZnIn₂S₄ onto g-C₃N₄ nanosheets, the SPS signal in the region from 300 to 450 nm is remarkably enlarged, suggesting the promoted charge generation and separation based on the semiconductor heterojunction effect. This phenomenon can be further understood through the steady-state and transient PL spectroscopy. In Figure 6B, the pure g-C₃N₄ nanosheet shows a strong emission peak with the center at ~450 nm. However, as compared to the g-C₃N₄ nanosheets, the emission process of ZnIn₂S₄/g-C₃N₄ heterojunction nanosheets suppresses significantly, revealing either the faster migration process with the shorter lifetime or the slower recombination process with the longer lifetime for the photoinduced charge carriers. To shed more light on this issue, we tried to fit the time-resolved transient PL spectroscopy based on the multi-exponential kinetics function expressed as follow⁴³:

$$I(t) = A_1 \cdot \exp(-t/\tau_1) + A_2 \cdot \exp(-t/\tau_2) \quad (1)$$

where τ_1 and τ_2 are the fluorescent lifetime, and A_1 and A_2 are the corresponding amplitudes. As listed in the insets of Fig. 6C,D, the short lifetime component for τ_1 is originated from the nonradiative recombination of charge-carriers in the defect states of g-C₃N₄, while the longer lifetime component for τ_2 is caused by the free excitons recombination in the g-C₃N₄ body^{12,21,34,42}. In the case of ZnIn₂S₄/g-C₃N₄ heterojunction nanosheets, the emission lifetime for the component τ_1 (3.3 ns) is longer than the corresponding lifetime of g-C₃N₄ nanosheets (3.1 ns), while its component τ_2 (12.3 ns) is shorter than the component for g-C₃N₄ nanosheets (14.7 ns). To gain further understanding on this phenomenon, the average emission lifetimes, relating to the overall emission decay behaviors of the samples, were also evaluated through the following equation⁴⁴:

$$\tau_A = \frac{A_1 \cdot \tau_1^2 + A_2 \cdot \tau_2^2}{A_1 \cdot \tau_1 + A_2 \cdot \tau_2} \quad (2)$$

It is clearly that after loading the ZnIn₂S₄ nanosheets, the average lifetime of g-C₃N₄ nanosheets is shortened from 10.45 ns to 8.97 ns. The combination of decreased emission lifetime and quenched PL indicates the emergence of a nonradiative pathway from the electron transfer between ZnIn₂S₄ and g-C₃N₄ nanosheets⁴⁵. According to the energy band structures of these semiconductors (Fig. 6E), it could be deduced that the photoinduced electrons transfer from the conduction band (CB) of g-C₃N₄ to the CB of ZnIn₂S₄ nanosheets. This assumption is in agreement with the emission quenching phenomenon of g-C₃N₄ nanosheets after decorating the ZnIn₂S₄ nanosheets. The rate constant for the interfacial electron-transfer (k_{et}) can be estimated by the expression⁴⁶:

$$k_{et}(g - C_3N_4 \rightarrow ZnIn_2S_4) = \frac{1}{\langle \tau_A \rangle_{(ZnIn_2S_4/g-C_3N_4)}} - \frac{1}{\langle \tau_A \rangle_{(g-C_3N_4)}} \quad (3)$$

Obviously, the k_{et} value is approximately $\sim 1.6 \times 10^7 \text{ s}^{-1}$. As illustrated in Fig. 6E, the CB and valence band (VB) positions of g-C₃N₄ straddle those of ZnIn₂S₄, forming the “type I” heterojunction interface. When this heterojunction is excited by visible light with the photon energy higher or equal to the band gaps of both ZnIn₂S₄ and g-C₃N₄ nanosheets, the photoinduced electrons and holes of g-C₃N₄ nanosheets would move to the CB and VB of ZnIn₂S₄ nanosheets, respectively. As such, the recombination process on the photoinduced charge carriers of g-C₃N₄ could be suppressed effectively by the photosynergistic effect of ZnIn₂S₄/g-C₃N₄ heterojunction. Accordingly, the amount of photoinduced charge carriers on ZnIn₂S₄ is remarkably increased based on the photoinduced interfacial charge transfer. During the photocatalytic H₂ production process, the photoinduced electrons accumulated on the CB of ZnIn₂S₄ could initiate the catalytic proton reduction to H₂. Accordingly, the photoinduced holes transfer from the VB of g-C₃N₄ to the VB of ZnIn₂S₄ were quenched by the sacrificial reagent of TEOA (or directly quenched by the sacrificial reagent on the VB of g-C₃N₄). In this way, the effective charge transfer at the interface between the ZnIn₂S₄ and g-C₃N₄ nanosheets results in the enhanced photocatalytic activity on H₂ production.

In summary, a series of ZnIn₂S₄/g-C₃N₄ heterojunction nanosheets with various contents of ZnIn₂S₄ have been successfully synthesized through *in-situ* growth of ultrathin ZnIn₂S₄ nanosheets onto g-C₃N₄ nanosheets fabricated by a traditional thermal polymerization and followed ultrasonic dispersion method. The unique “sheet-on-sheet” heterostructure obtained by vertically loading ZnIn₂S₄ nanosheets onto the g-C₃N₄ nanosheets surfaces leads to the enlarged reactive sites and enhanced light absorption ability. More importantly, the formation of “type I” heterojunction can effectively suppress the photoinduced charge recombination of g-C₃N₄ through the interfacial charge transfer, as evidenced by the electron microscopic analyses, steady-state and time-resolved transient photoluminescence decay investigations. As a result, the ZnIn₂S₄/g-C₃N₄ heterojunction nanosheets exhibited considerable enhancement on the photocatalytic activity for H₂ production as compared the single component nanosheets. It is believed that our study provides a promising strategy to develop the new generation of hierarchical heterostructure photocatalysts for highly efficient solar-to-fuels conversion and environmental remediation.

Methods

Materials synthesis. The graphitic carbon nitride (g-C₃N₄) was obtained by a traditional thermal polymerization method. 10 g of melamine powder was grinded for 60 min in a mortar and then transferred to an alumina crucible with a cover. Afterward, the crucible was heated to 550 °C with a rising rate of 20 °C min^{−1} and kept for 2 h at the required temperature under semiclosed environment, resulting in the bulk g-C₃N₄ with faint-yellow color. ZnIn₂S₄/g-C₃N₄ heterojunction nanosheets were synthesized by *in-situ* growth of ultrathin ZnIn₂S₄ nanosheets onto g-C₃N₄ nanosheets through a facile hydrothermal method. In a typical procedure, 600 mg of as-synthesized bulk g-C₃N₄ was grinded to fine powder and then added into 20 ml of methanol. After ultrasonic treatment for 2 h, the bulk g-C₃N₄ was exfoliated into thin nanosheets which was then collected and washed by using centrifugation-redispersion with deionized water. Subsequently, these exfoliated g-C₃N₄ nanosheets were resuspended into 20 ml of premade aqueous solution consisting of 0.2125 mmol of Zn(CH₃COO)₂ · 2H₂O, 0.425 mmol of In(NO₃)₃ · 6H₂O, and 1.7 mmol of L-cysteine. After being ultrasonically treated for 30 min, this mixture was transferred into a Teflon-lined stainless steel autoclave with a capacity of 25 mL. Afterward, the autoclave was sealed and maintained at 180 °C for 12 h in an electric oven. When natural cooling the autoclave to room temperature, the yellow-green suspension was collected, washed with ethanol and deionized water for several times, and finally dried in an electric oven at 60 °C for a night. Thus, the 15 wt% ZnIn₂S₄/g-C₃N₄ heterojunction nanosheets were synthesized. The pure ZnIn₂S₄ nanosheets were fabricated by the same hydrothermal conditions in the absence of the g-C₃N₄ nanosheets substrates. Meanwhile, to achieve the optimal photocatalytic activity, the ZnIn₂S₄/g-C₃N₄ heterojunction nanosheets with different ZnIn₂S₄ loading amount were also synthesized using the similar route by adjusting the concentrations of hydrothermal precursor solution in the same component ratios. In order to further prove that the enhanced photocatalytic activity of ZnIn₂S₄/g-C₃N₄ nanosheets is due to the heterojunction effect, another control sample were fabricated through hydrothermal treatment of pure g-C₃N₄ nanosheets in the absence of the above ZnIn₂S₄ precursors.

Characterization methods. X-ray diffraction (XRD) patterns of the as-synthesized samples were measured by a Shimadzu XRD-6000 X-ray diffractometer with a Cu K α line of 0.1541 nm. Scanning electron microscopy (SEM; XL-30 ESEM FEG, Micro FEI Philips) and transmission electron microscopy (TEM; JEOL JEM-2100) were employed to observe the morphologies and structures of the samples. Energy dispersive X-ray (EDX)

spectroscopy being attached to scanning electron microscopy (SEM) was used to analyze the composition of products. Fourier transform infrared (FT-IR) spectra were recorded on a Magna 560 FT-IR spectrometer with a resolution of 1 cm^{-1} . X-ray photoelectron spectroscopy (XPS) was carried out on a VG-ESCALAB LKII instrument with a Mg K α ADES ($h\nu = 1253.6\text{ eV}$) source at a residual gas pressure below 10^{-8} Pa . UV-vis diffuse reflectance spectra (DRS) were taken with a Lambda 750 UV/Vis/NIR spectrophotometer (Perkin Elmer, USA). The specific surface areas of the products were measured with a Micromeritics ASAP-2020 instrument and analyzed by the Brunauer–Emmett–Teller (BET) method. Decay curves of the as-fabricated products were obtained on a FLS920 fluorescence lifetime spectrophotometer (Edinburgh Instruments, UK) under the excitation of a hydrogen flash lamp with the wavelength at 325 nm (nF900; Edinburgh Instruments). The surface photovoltage spectroscopy (SPS) was performed on PL-SPS1000 instrument (Beijing Perfectlight Technology Co., Ltd). During the process, the sample was put between the indium tin oxide (ITO) glass and stainless steel electrodes to form a sandwich structured photovoltage cell.

Photocatalytic H_2 production. The photocatalytic H_2 production tests were performed in a 35-mL quartz reactor. Typically, 5 mg of the as-synthesized samples were suspended in 10-mL triethanolamine (TEOA, 15 vol.%) aqueous solution. This suspension was sealed in the quartz reactor by a rubber plug, and then purged with argon gas for half an hour to drive away the residual air. Subsequently, the reactor was exposed under a 300-W Xe lamp (PLS-SXE300UV) coupled with a 400 nm cut-off filter. The gas product composition from the upper space above the liquid in the quartz reactor was periodically analyzed by a gas chromatograph (GC) equipped with a thermal conductivity detector (TCD) (Beifen-Ruili Analytical Instrument, SP-3420A). The apparent quantum efficiency (QE) was estimated by using the following equation.

$$\text{AQE} = \frac{2 \times \text{number of evolved hydrogen molecules}}{\text{number of incident photons}} \times 100\%$$

References

1. Liu, J. *et al.* Metal-free efficient photocatalyst for stable visible water splitting via a two-electron pathway. *Science* **347**, 970–974 (2015).
2. Jing, L., Zhou, W., Tian, G. & Fu, H. Surface tuning for oxide-based nanomaterials as efficient photocatalysts. *Chem. Soc. Rev.* **42**, 9509–9549 (2013).
3. Ran, J., Zhang, J., Yu, J., Jaroniec, M. & Qiao, S. Z. Earth-abundant cocatalysts for semiconductor-based photocatalytic water splitting. *Chem. Soc. Rev.* **43**, 7787–7812 (2014).
4. Ma, Y. *et al.* Titanium Dioxide-Based Nanomaterials for Photocatalytic Fuel Generations. *Chem. Rev.* **114**, 9987–10043 (2014).
5. Yu, J. & Ran, J. Facile preparation and enhanced photocatalytic H_2 -production activity of $\text{Cu}(\text{OH})_2$ cluster modified TiO_2 . *Energy Environ. Sci.* **4**, 1364–1371 (2011).
6. Manikandan, M. *et al.* Photocatalytic Water Splitting under Visible Light by Mixed-Valence Sn_3O_4 . *ACS Appl. Mater. Interfaces* **6**, 3790–3793 (2014).
7. Zhang, J. *et al.* Efficient Visible-Light Photocatalytic Hydrogen Evolution and Enhanced Photostability of Core/Shell $\text{CdS/g-C}_3\text{N}_4$ Nanowires. *ACS Appl. Mater. Interfaces* **5**, 10317–10324 (2013).
8. Sun, S. Recent advances in hybrid Cu_2O -based heterogeneous nanostructures. *Nanoscale* **7**, 10850–10882 (2015).
9. Yu, C., Li, G., Kumar, S., Yang, K. & Jin, R. Phase transformation synthesis of novel $\text{Ag}_2\text{O/Ag}_2\text{CO}_3$ heterostructures with high visible light efficiency in photocatalytic degradation of pollutants. *Adv. Mater.* **26**, 892–898 (2014).
10. Liu, Y., Zhang, M., Li, L. & Zhang, X. One-dimensional visible-light-driven bifunctional photocatalysts based on $\text{Bi}_4\text{Ti}_3\text{O}_{12}$ nanofiber frameworks and Bi_2XO_6 ($\text{X} = \text{Mo}, \text{W}$) nanosheets. *Appl. Catal. B* **160–161**, 757–766 (2014).
11. Wang, X. *et al.* A metal-free polymeric photocatalyst for hydrogen production from water under visible light. *Nature Chem.* **8**, 76–80 (2009).
12. Wang, R. *et al.* Quasi-Polymeric Metal-Organic Framework $\text{UiO}-66/\text{g-C}_3\text{N}_4$ Heterojunctions for Enhanced Photocatalytic Hydrogen Evolution under Visible Light Irradiation. *Adv. Mater. Interfaces* **10**, 1002/admi.201500037 (2015).
13. Yuan, Y.-P. *et al.* Improving photocatalytic hydrogen production of metal-organic framework $\text{UiO}-66$ octahedrons by dye-sensitization. *Appl. Catal. B* **168–169**, 572–576 (2015).
14. Han, X.-B. *et al.* Polyoxometalate-Based Nickel Clusters as Visible Light-Driven Water Oxidation Catalysts. *J. Am. Chem. Soc.* **137**, 5486–5493 (2015).
15. Cao, S. & Yu, J. $\text{g-C}_3\text{N}_4$ -Based Photocatalysts for Hydrogen Generation. *J. Phys. Chem. Lett.* **5**, 2101–2107 (2014).
16. Yuan, Y.-P. *et al.* Microwave-assisted heating synthesis: a general and rapid strategy for large-scale production of highly crystalline $\text{g-C}_3\text{N}_4$ with enhanced photocatalytic H_2 production. *Green Chem.* **16**, 4663–4668 (2014).
17. Cao, S., Low, J., Yu, J. & Jaroniec, M. Polymeric Photocatalysts Based on Graphitic Carbon Nitride. *Adv. Mater.* **27**, 2150–2176 (2015).
18. Niu, P., Yin, L., Yang, Y., Liu, G. & Cheng, H. Increasing the Visible Light Absorption of Graphitic Carbon Nitride (Melon) Photocatalysts by Homogeneous Self-Modification with Nitrogen Vacancies. *Adv. Mater.* **26**, 8046–8052 (2014).
19. Kang, Y. *et al.* An Amorphous Carbon Nitride Photocatalyst with Greatly Extended Visible-Light-Responsive Range for Photocatalytic Hydrogen Generation. *Adv. Mater.* **27**, 4572–4577 (2015).
20. Cao, S.-W. *et al.* Artificial photosynthetic hydrogen evolution over $\text{g-C}_3\text{N}_4$ nanosheets coupled with cobaloxime. *Phys. Chem. Chem. Phys.* **15**, 18363–18366 (2013).
21. Zhang, Z., Huang, J., Zhang, M., Yuan, Q. & Dong, B. Ultrathin hexagonal SnS_2 nanosheets coupled with $\text{g-C}_3\text{N}_4$ nanosheets as 2D/2D heterojunction photocatalysts toward high photocatalytic activity. *Appl. Catal. B* **163**, 298–305 (2015).
22. Zhang, Z., Huang, J., Yuan, Q. & Dong, B. Intercalated graphitic carbon nitride: a fascinating two-dimensional nanomaterial for an ultra-sensitive humidity nanosensor. *Nanoscale* **6**, 9250–9256 (2014).
23. Yuan, Y.-P., Cao, S.-W., Liao, Y.-S., Yin, L.-S. & Xue, C. Red phosphor/ $\text{g-C}_3\text{N}_4$ heterojunction with enhanced photocatalytic activities for solar fuels production. *Appl. Catal. B* **140–141**, 164–168 (2013).
24. Li, X. *et al.* Engineering heterogeneous semiconductors for solar water splitting. *J. Mater. Chem. A* **3**, 2485–2534 (2015).
25. Ye, L., Fu, J., Xu, Z., Yuan, R. & Li, Z. Facile One-Pot Solvothermal Method to Synthesize Sheet-on-Sheet Reduced Graphene Oxide (RGO)/ ZnIn_2S_4 Nanocomposites with Superior Photocatalytic Performance. *ACS Appl. Mater. Interfaces* **6**, 3483–3490 (2014).
26. Zhang, P. *et al.* Bi_2MoO_6 ultrathin nanosheets on ZnTiO_3 nanofibers: A 3D open hierarchical heterostructures synergistic system with enhanced visible-light-driven photocatalytic activity. *J. Hazard. Mater.* **217–218**, 422–428 (2012).
27. Liu, Y., Zhang, M. Y., Li, L. & Zhang, X. T. One-dimensional visible-light-driven bifunctional photocatalysts based on $\text{Bi}_4\text{Ti}_3\text{O}_{12}$ nanofiber frameworks and Bi_2XO_6 ($\text{X} = \text{Mo}, \text{W}$) nanosheets. *Appl. Catal. B* **160–161**, 757–766 (2014).

28. Chen, Y. *et al.* Exploring the Different Photocatalytic Performance for Dye Degradations over Hexagonal ZnIn_2S_4 Microspheres and Cubic ZnIn_2S_4 Nanoparticles. *ACS Appl. Mater. Interfaces* **4**, 2273–2279 (2012).
29. Zhou, J. *et al.* *In situ* controlled growth of ZnIn_2S_4 nanosheets on reduced graphene oxide for enhanced photocatalytic hydrogen production performance. *Chem. Commun.* **49**, 2237–2239 (2013).
30. Shang, L. *et al.* Facile synthesis of hierarchical ZnIn_2S_4 submicrospheres composed of ultrathin mesoporous nanosheets as a highly efficient visible-light-driven photocatalyst for H_2 production. *J. Mater. Chem. A* **1**, 4552–4558 (2013).
31. Chen, Y. *et al.* Hierarchical Core–Shell Carbon Nanofiber@ ZnIn_2S_4 Composites for Enhanced Hydrogen Evolution Performance. *ACS Appl. Mater. Interfaces* **6**, 13841–13849 (2014).
32. Mandal, L., Chaudhari, N. S. & Ogale, S. Self-Powered UV-vis Photodetector Based on ZnIn_2S_4 /Hydrogel Interface. *ACS Appl. Mater. Interfaces* **5**, 9141–9147 (2013).
33. Liu, Q. *et al.* 2D ZnIn_2S_4 Nanosheet/1D TiO_2 Nanorod Heterostructure Arrays for Improved Photoelectrochemical Water Splitting. *ACS Appl. Mater. Interfaces* **6**, 17200–17207 (2014).
34. Zhang, Z. *et al.* Multichannel-Improved Charge Carrier Dynamics in Well-Designed Hetero-Nanostructural Plasmonic Photocatalysts Toward Highly Efficient Solar-to-Fuels Conversion. *Adv. Mater.* **27**, 5906–5914 (2015).
35. Wang, X., Chen, X., Thomas, A., Fu, X. & Antonietti, M. Metal-Containing Carbon Nitride Compounds: A New Functional Organic-Metal Hybrid Material. *Adv. Mater.* **21**, 1609–1612 (2009).
36. Liu, J., Zhang, T., Wang, Z., Dawson, G. & Chen, W. Simple pyrolysis of urea into graphitic carbon nitride with recyclable adsorption and photocatalytic activity. *J. Mater. Chem.* **21**, 14398–14401 (2011).
37. Zhang, Z. *et al.* Electrospun Nanofibers of p-Type NiO /n-Type ZnO Heterojunctions with Enhanced Photocatalytic Activity. *ACS Appl. Mater. Interfaces* **2**, 2915–2923 (2010).
38. Zhang, Z. *et al.* Hierarchical assembly of ultrathin hexagonal SnS_2 nanosheets onto electrospun TiO_2 nanofibers: enhanced photocatalytic activity based on photoinduced interfacial charge transfer. *Nanoscale* **5**, 606–618 (2013).
39. Li, X. H. *et al.* Local chemical states and thermal stabilities of nitrogen dopants in ZnO film studied by temperature-dependent x-ray photoelectron spectroscopy. *Appl. Phys. Lett.* **95**, 191903 (2009).
40. Xiang, Q., Yu, J. & Jaroniec, M. Preparation and Enhanced Visible-Light Photocatalytic H_2 -Production Activity of Graphene/ C_3N_4 Composites. *J. Phys. Chem. C* **115**, 7355–7363 (2011).
41. Cao, S.-W. *et al.* *In-situ* growth of CdS quantum dots on g- C_3N_4 nanosheets for highly efficient photocatalytic hydrogen generation under visible light irradiation. *Int. J. Hydrogen Energy* **38**, 1258–1266 (2013).
42. Cao, S.-W. *et al.* Solar-to-fuels conversion over In_2O_3 /g- C_3N_4 hybrid photocatalysts. *Appl. Catal. B* **147**, 940–946 (2014).
43. Wang, X. *et al.* Engineering Interfacial Photo-Induced Charge Transfer Based on Nanobamboo Array Architecture for Efficient Solar-to-Chemical Energy Conversion. *Adv. Mater.* **27**, 2207–2214 (2015).
44. Chen, Y.-C., Pu, Y.-C. & Hsu, Y.-J. Interfacial Charge Carrier Dynamics of the Three-Component In_2O_3 - TiO_2 -Pt Heterojunction System. *J. Phys. Chem. C* **116**, 2967–2975 (2012).
45. Bian, Z., Tachikawa, T., Kim, W., Choi, W. & Majima, T. Superior Electron Transport and Photocatalytic Abilities of Metal-Nanoparticle-Loaded TiO_2 Superstructures. *J. Phys. Chem. C* **116**, 25444–25453 (2012).
46. Yang, T.-T. *et al.* Interfacial Charge Carrier Dynamics in Core-Shell Au-CdS Nanocrystals. *J. Phys. Chem. C* **114**, 11414–11420 (2010).

Acknowledgements

This work is supported by the National Natural Science Foundation of China (grant nos 51402038, 11474046, and 11274057), Program for New Century Excellent Talents in University (NCET-13-0702), Technology Foundation for Selected Overseas Chinese Scholar from Ministry of Personnel of China, Scientific Research Foundation for Doctor of Liaoning Province (grant no. 20141118), Educational Committee Foundation of Liaoning Province (grant no. L2014547), Science and Technology Project of Liaoning Province (grant no. 2012222009), Program for Liaoning Excellent Talents in University (LNET) (grant no. LJQ2012112), Fundamental Research Funds for the Central Universities (grant nos DC201502080203 and DC201502080304), and Science and Technique Foundation of Dalian (grant no. 2013A14GX040).

Author Contributions

Z.Z. and B.D. proposed and guided the overall project. Z.Z. carried out the major part of experiments and results analyses. K.L., Z.F. and Y.B. assisted Z.Z. to perform the materials characterizations. Z.Z. wrote the manuscript with discussion from all authors. All authors reviewed the manuscript.

Additional Information

Supplementary information accompanies this paper at <http://www.nature.com/srep>

Competing financial interests: The authors declare no competing financial interests.

How to cite this article: Zhang, Z. *et al.* Hierarchical Sheet-on-Sheet ZnIn_2S_4 /g- C_3N_4 Heterostructure with Highly Efficient Photocatalytic H_2 production Based on Photoinduced Interfacial Charge Transfer. *Sci. Rep.* **6**, 19221; doi: 10.1038/srep19221 (2016).



This work is licensed under a Creative Commons Attribution 4.0 International License. The images or other third party material in this article are included in the article's Creative Commons license, unless indicated otherwise in the credit line; if the material is not included under the Creative Commons license, users will need to obtain permission from the license holder to reproduce the material. To view a copy of this license, visit <http://creativecommons.org/licenses/by/4.0/>